Designing plasmonic eigenstates for optical signal transmission in planar channel devices

Upkar Kumar,[1] Sviatlana Viarbitskaya,[2] Christian Girard,[1] Aurélien Cuche,[1] Sreenath Bolisetty,[3] Raffaele Mezzenga,[3] Gérard Colas des Francs,[2] Alexandre Bouhelier,[2] * Erik Dujardin[1] *

[1] *CEMES CNRS UPR 8011, 29 rue J. Marvig, 31055 Toulouse, France.*

[2] *LICB, CNRS UMR 6303, Université de Bourgogne, 9 Av. A. Savary, Dijon, France.*

[3] *ETH Zurich, Department of Health Sciences and Technology, Schmelzberg-strasse 9, CH-8092 Zurich, Switzerland*

* Corresponding author: dujardin@cemes.fr

Supplementary information

Table of contents

S1. Diabolo nanofabrication from single crystalline Au microplatelets

The diabolo-shaped transmission devices were produced from crystalline gold microplates deposited on ITO-coated glass coverslip as described in the Methods section.
The large polydispersity of the colloidal suspension allowed to easily select hexagonal plates of adequate sizes (typically 3-5 micrometer diameter) that could be located optically or in the electron microscope with respect to labelled crossmarks (Fig. S1a and S1b).
The Ga ion milling is performed in two stages. First, the structure is defined and isolated by a sequence of irradiation boxes optimized to reduce the edge amorphisation and metal redeposition (Fig. S1c). Then the peripheral areas of the starting platelet are removed leaving an isolated structure on the ITO/glass substrate (Fig. S1d).
Figures S1e to h show a series of several diabolo structures fabricated and studied in this work.
The fabrication protocol is also illustrated by the movie provided as a separate supplementary material.

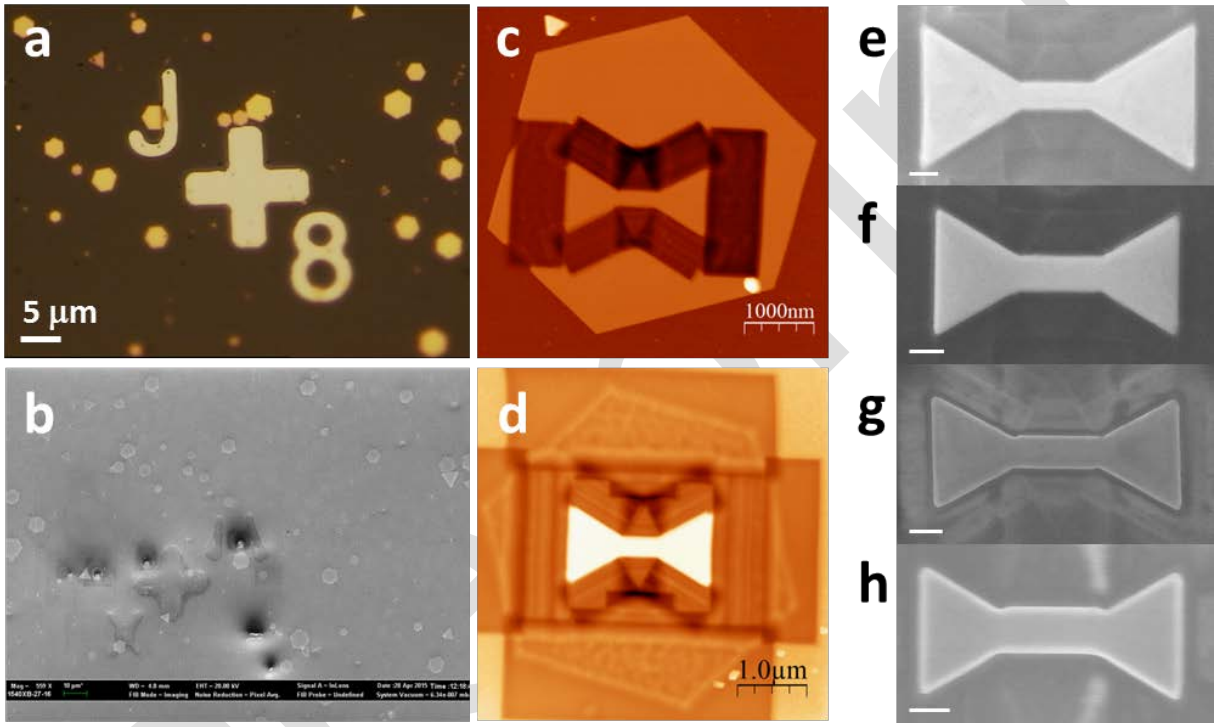

Figure S1: Diabolo nanofabrication. (a) Optical and (b) electronic images of the cross-marked ITO substrate bearing Au microplatelets. (c) AFM image recorded after the first FIB milling step and showing the diabolo structure defined inside a 5-µm diameter hexagonal platelet. (d) AFM image of the same sample after the second step dedicated to the removal of the peripheral Au platelet areas. (e-h) SEM images of several diabolo structures with different triangular pad sizes and channel dimensions. Scale bars are 200 nm.

S2. Confocal and Image plane TPL mapping

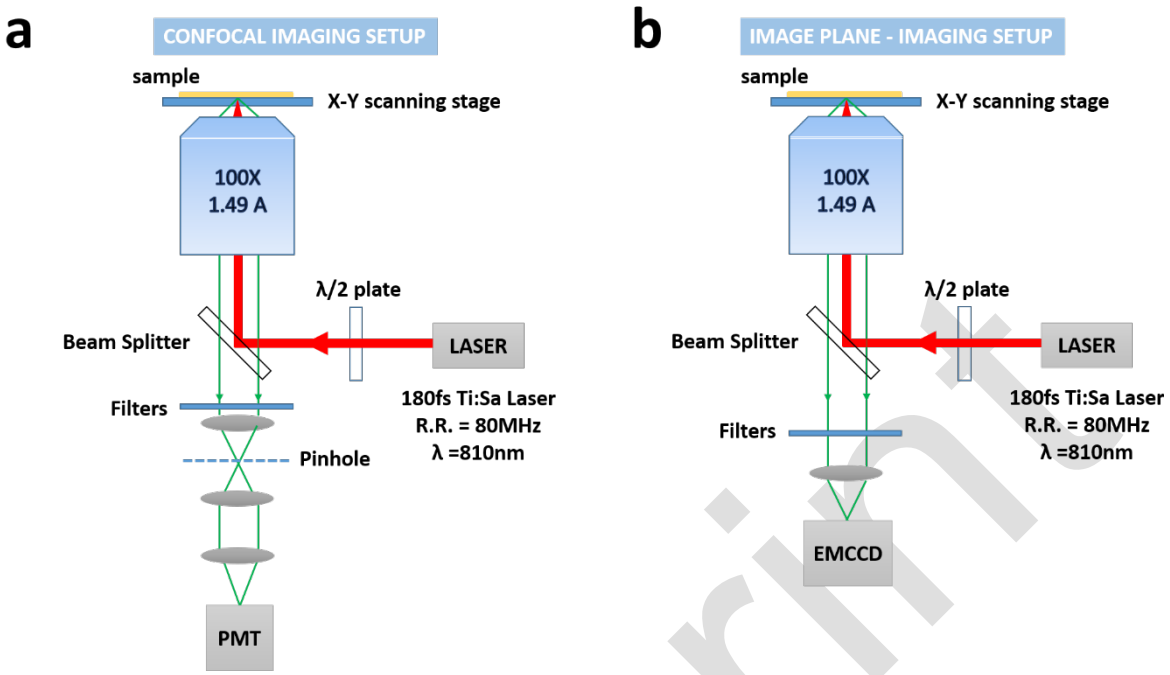

Figure S2: Schematics of experimental set-ups for (a) confocal TPL mapping and (b) image plane non-linear photoluminescence (nPL) mapping

S3 SPLDOS, simulated and experimental confocal TPL maps

Confocal two-photon luminescence (TPL) mapping visualizes the spatial distribution of the surface plasmon local density of states (SPLDOS) as demonstrated in refs [1-3]. Here we apply confocal TPL mapping to diabolo structures and we evidence modal behavior reminiscent to the one displayed by triangular nanoprisms. Experimental maps are compared to simulated TPL and SPLDOS maps using the tools developed and described in our earlier work.

In particular, the SPLDOS and TPL patterns generated by the symmetrical diabolo structure shown in Fig. S1e are displayed in Fig S3 for four different incident linear polarizations. Fig. S3a to S3d are the maps of the partial SPLDOS at 810 nm projected on the polarization direction 0°, 90°, 120° and 150° with respect to horizontal. Our Green Dyadic Method code is used to simulate the realistic confocal TPL response (beam waist 250 nm) at 810 nm excitation for these four linear polarizations (Fig. S3e-S3h). These simulated maps can be compared to the experimental ones (Fig. S3i-S3l) acquired by raster scanning the 300-nm focused beam waist of the pulsed Ti : Sapphire laser operated at 810 nm and by collecting the non-linear luminescence signal (cut-off filter at 500 nm). Both experimental and simulated TPL maps patterns match and relative intensities on the apexes and in the channel recorded experimentally are well accounted for in the simulations.

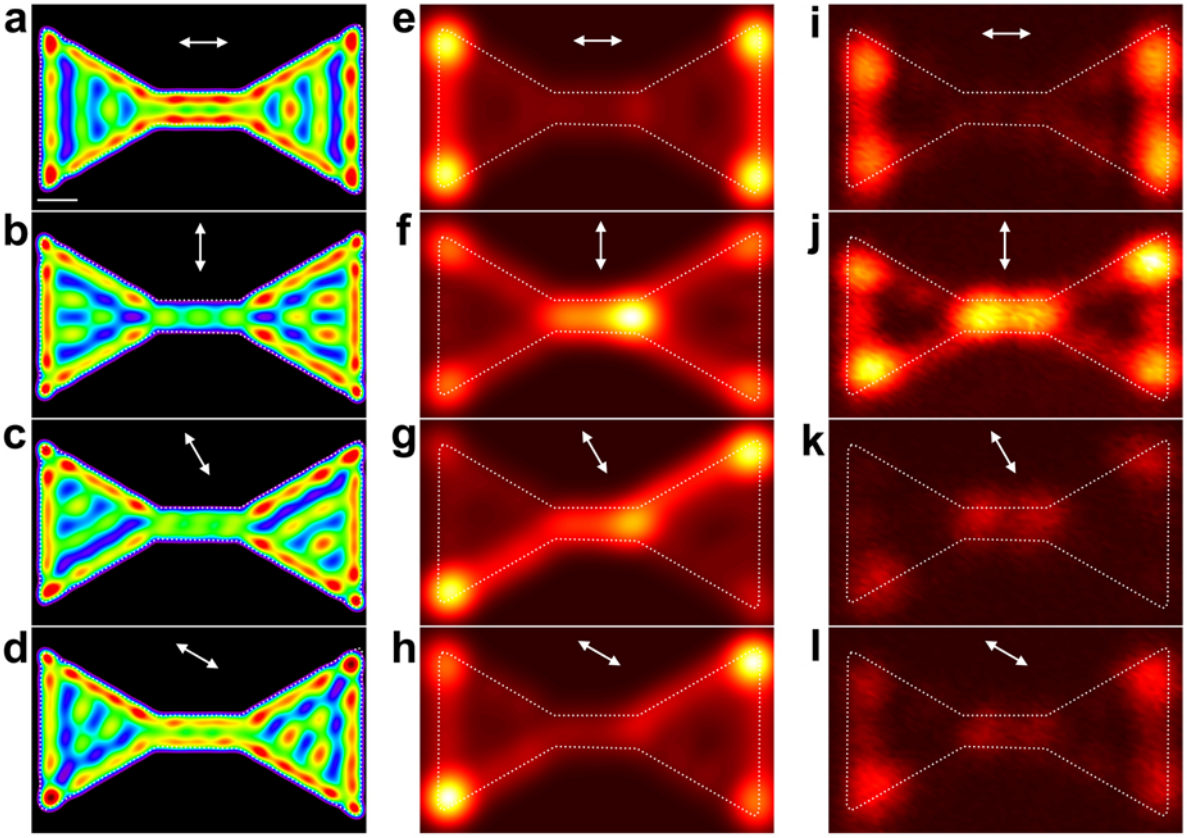

Figure S3. (a-d) Partial SPLDOS maps at 810 nm, obtained for projection along the (a) 0°, (b) 90°, (c) 120°,(d) 150° polarization directions. (e-h) Simulated confocal TPL maps for an excitation at 810 nm, with a realistic beam waist of the incident Gaussian beam of 250 nm diameter. (i-l) Experimental confocal maps recorded for the same corresponding polarization directions. The sample is described in Fig. 2.

The observation of intense and sharply localized luminescence spots at the outer apexes of the triangular pads, the intensity of which is modulated upon rotating the excitation polarization direction, is reminiscent of our earlier reports on the non-linear patterns produced by triangular nanoprisms. In particular, the longitudinal excitation (0° polarization; Figs. S3a, S3e and S3i) is associated with a

minimal confocal signal in the channel and a maximal intensity emitted from the outer apexes. On the contrary, the transverse excitation (90° polarization; Figs. S3b, S3f and S3j) exhibits a reinforcement of the confocal emission localized in the channel. Intermediate projections, such as the one shown in Figs. S3c, S3g and S3k (polarization angle 120°) indicate that high TPL (i.e. high SPLDOS) is distributed along a path connecting one apex on the left triangular pad to the opposite apex on the right pad, through the channel.

The exact same observations are made for the diabolo presented in Figure 2 of the main text. The SPLDOS and simulated TPL are shown in Fig. 3 and match the corresponding experimental confocal TPL displayed in Fig. S4. However, one can notice one bright spot on the lower edge of the right triangular pad is always visible in the confocal maps, irrespective of the excitation polarization direction, and is attributed to a small defect in the substrate near the diabolo. Such a defect does not affect transmittance when the diabolo is excited far from the defect (in position (I) for example) and the signal collected in leakage image plane mapping. This indicates that the defect might not be directly connected to the diabolo structure but within a spot radius when the confocal detection is recorded close to the channel entrance. Incidentally, this defect close but not on the diabolo may explain the small but real asymmetry observed in image plane maps recorded when exciting in Ci (Figs. 4b and 4d) that are not accounted for by the simulation on the realistic model (Figs. 4a and 4c). Indeed when exciting in Ci, the defect may be excited alongside and generate a non-symmetrical input configuration.

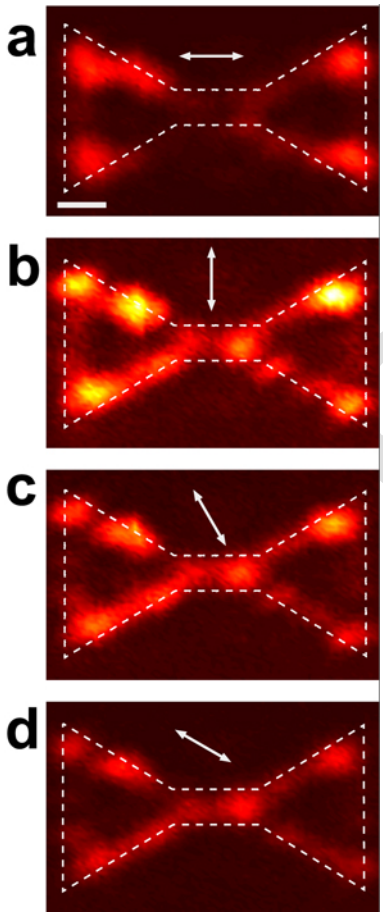

Figure S4. Confocal TPL maps recorded at (a) 0°, (b) 90°, (c) 120°, (d) 150° in-plane polarization respectively with an 810-nm excitation of the diabolo structure described in Figure 2. Common scale bar is 200 nm.

S4 Polarization dependency of the TPL intensity in image plane maps

The transmittance through the diabolo structure is highly modulated by the excitation polarization direction (See Figs. 1, 2, 4). In Figure S5, we show the full polarization dependency of the signal recorded on image plane TPL maps at the location of the excitation beam (Input I), at the channel entrance (Ci) and at the readout output (O) for the symmetrical (Fig. S5a) and non-symmetrical (Fig. S5b) diabolos studied in the main text.

In Figure 6a, one observes that the TPL signal is alternatively maximum above each successive apex (the first being (I), the second one being the channel input Ci and the third one being the lower apex). Strikingly, the output (O) polarization dependency strictly matches the one in (Ci). The maximum intensity on (I), (Ci) and the lower apex are shifted by about 80°-90°. This graph suggest that the transmittance remains low for most polarization configurations until the channel is adequately excited – for angles close to 0° - and then the funneling as far as the the output (O) is set without further polarization shift (red and blue curves overlap). This behavior indicates the excitation of a resonance mode delocalized over the 2D diabolo structure that is characterized by a sharp polarization-dependent condition.

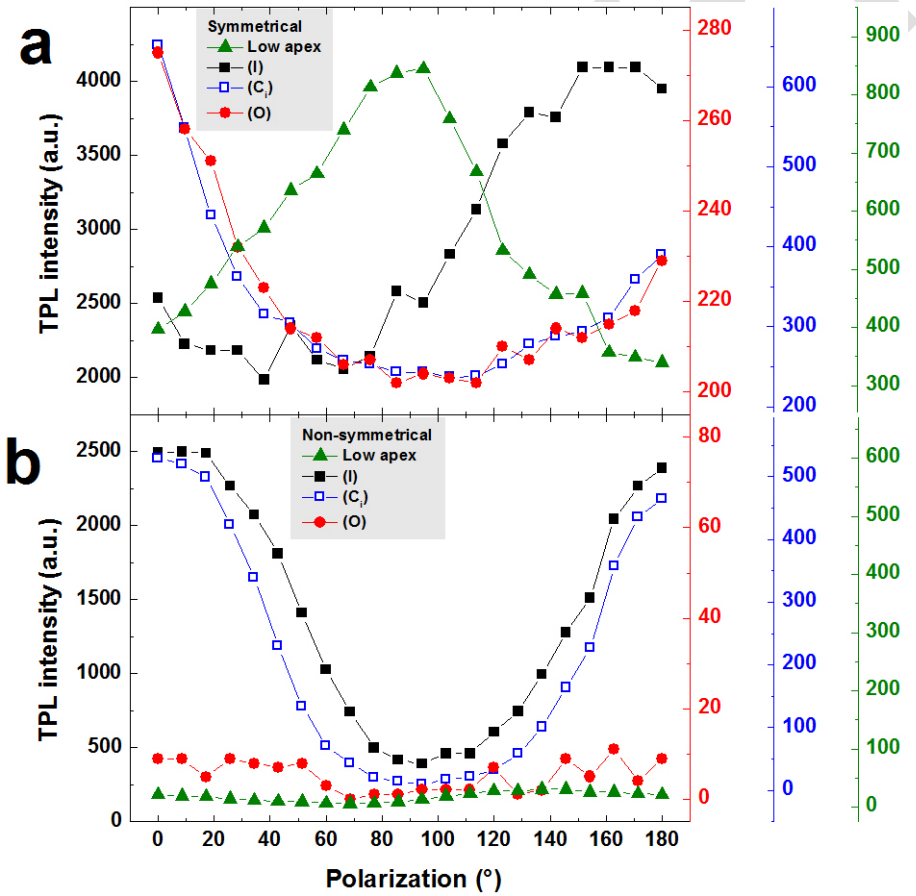

Figure S5. Evolution of the TPL intensity recorded in points I (black squares), Cᵢ (blue open squares), O (red dots) and the lower apex of the excited triangular pad (green triangles) from the image plane maps obtained for an excitation in (I) with the polarization direction between 0° and 180° with respect to the diabolo main axis. Panel (a) refers to the symmetrical diabolo shown in Fig. 2a and panel (b) refers to the non-symmetrical diabolo shown in Fig. 4a. Each dataset has its own color-coded Y-scale. Note that the amplitude of the scales for a given point are close to identical between panels (a) and (b) for relative comparison but the origins have been slightly shifted for clarity.

On the contrary, the transmittance intensity along the non-symmetrical diabolo shows a perfectly overlapping polarization evolution in (I) and (Ci) suggesting a global non-resonant modulation. The third

apex and the output remain close to their minimal value with a very small modulation also in phase. When excited at 810 nm, the asymmetrical produces a transmitted luminescence that is spatially attenuated (See Fig 5) and modulated uniformly by the incident polarization.

The polarization dependency reported here reinforce the attribution of the effective transmittance to the excitation of a delocalized SP mode that display SPLDOS intensity extrema at opposite apexes used as input (I) and output (O).

S5 Calculation of near-field transmittance maps and spectra

Here, we describe the numerical tool based on the Green dyadic formalism that provides the computation of the electric field transfer between two remote locations in an arbitrary shaped metallic nanostructure as illustrated in Figure S6.

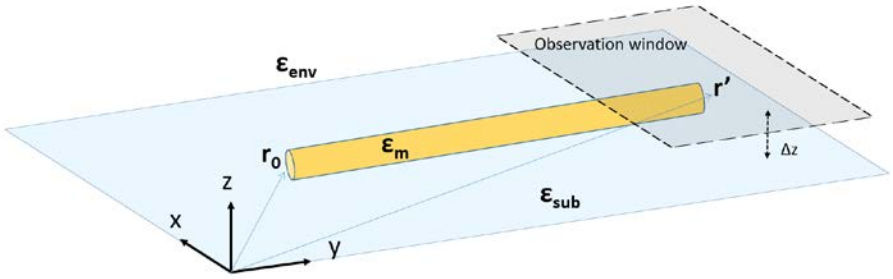

Figure S6. Schematic geometry of a plasmonic 1D channel, supported by a transparent dielectric substrate, and the associated observation window above the structure used for simulations. The size of this window can be adjusted to the dimensions of the structure.

In a metallic system where surface plasmons can be excited by a focused illumination $\mathbf{E_0}$, of angular frequency ω and positioned at $\mathbf{r_0}$, the expression of the electric field $\mathbf{E_{out}}$ at a given output location **r'** can be expressed as follows:[4,5]

$$\boldsymbol{E_{out}}(\boldsymbol{r'}, \boldsymbol{r_0}, \omega) = \int_V \boldsymbol{K}(\boldsymbol{r'}, \boldsymbol{r}, \omega).\boldsymbol{E_0}(\boldsymbol{r}, \boldsymbol{r_0}, \omega)\, d\boldsymbol{r} \qquad \textbf{(1)}$$

where *V* is the volume of the metallic object, and $\boldsymbol{K}(\mathbf{r'}, \mathbf{r}, \omega)$ is the generalized field propagator that contains the entire response of the sample under any incident illumination:[4]

$$\boldsymbol{K}(\boldsymbol{r'}, \boldsymbol{r}, \omega) = \delta(\boldsymbol{r} - \boldsymbol{r'}) + \chi(\boldsymbol{r}, \omega).\boldsymbol{S}(\boldsymbol{r'}, \boldsymbol{r}, \omega) \qquad \textbf{(2)}$$

$\boldsymbol{S}(\mathbf{r'}, \mathbf{r}, \omega)$ is the Green Dyadic tensor describing the whole system that includes the plasmonic structure and the dielectric substrate. In addition, the frequency-dependent optical response of the metallic structure is given by:

$$\chi(\boldsymbol{r}, \omega) = \frac{\varepsilon_m(r,\omega) - \varepsilon_{env}}{4\pi} \text{ in the metal,} \qquad \textbf{(3)}$$

and $\chi(\boldsymbol{r}, \omega) = 0$ outside of the metallic object.

In this work, we focused on the plasmon-mediated field transfer in the metallic structures. We therefore excluded the direct contribution of the incident illumination at the output location.[6] This can be done by removing the delta Dirac distribution in equation ***(2)***:

$$\boldsymbol{K}(\boldsymbol{r'}, \boldsymbol{r}, \omega) = \chi(\boldsymbol{r}, \omega).\boldsymbol{S}(\boldsymbol{r'}, \boldsymbol{r}, \omega) \qquad \textbf{(4)}$$

The whole set of experimental data presented in this study has been acquired using a focused Gaussian illumination. Consequently, the illumination field $\mathbf{E_0}$ has been modelled as a Gaussian spot through an expansion in a plane waves in the wave vector domain:[7-10]

$$\boldsymbol{E_0}(\boldsymbol{r}, \boldsymbol{r_0}, \omega) = \int_{-\sqrt{\varepsilon_{sub}}k_0}^{\sqrt{\varepsilon_{sub}}k_0} d\alpha \int_{-\sqrt{\varepsilon_{sub}k_0^2 - \alpha^2}}^{\sqrt{\varepsilon_{sub}k_0^2 - \alpha^2}} d\beta\, \boldsymbol{\zeta} exp\left[-\frac{w_0^2(\alpha^2+\beta^2)}{4}\right] exp\left[i\alpha(x - x_0) + i\beta(x - y_0) + ik_z(x - z_0)\right],$$

(5)

k_0 is the vacuum wave vector of the incident light and $\boldsymbol{r_0} = (x_0, y_0, z_0)$ defines the center of the excitation Gaussian spot in the Cartesian system of coordinates shown in Fig. S6. ε_{sub} is the dielectric function of the substrate and the beam waist w_0 describes the lateral extension of this incident Gaussian beam. The integration in equation ***(5)*** is performed in the 2D reciprocal space defined by the vector $\boldsymbol{k_{//}} = (\alpha, \beta)$. In order to take into account the realistic geometry of the system with a transparent substrate, the tangential components of the field vector ζ are expressed as follows:

$$\begin{pmatrix} \zeta_x \\ \zeta_y \end{pmatrix} = \mathrm{T} \begin{pmatrix} E_{0,x} \\ E_{0,y} \end{pmatrix}, \qquad \textbf{(6)}$$

The transmission matrix T reads:

$$\mathrm{T} = \begin{pmatrix} (\tau_{\parallel} - \tau_{\perp})\cos^2\delta + \tau_{\perp} & (\tau_{\parallel} - \tau_{\perp})\cos\delta\sin\delta \\ (\tau_{\parallel} - \tau_{\perp})\cos\delta\sin\delta & (\tau_{\parallel} - \tau_{\perp})\sin^2\delta + \tau_{\perp} \end{pmatrix}, \qquad \textbf{(7)}$$

$\tau_{\parallel}$ and $\tau_{\perp}$ are the Fresnel coefficients for the interface. Here, δ is an angle in the xy plane between the x-axis in Cartesian coordinates and the orientation of the planar component of the wave vector $\boldsymbol{k_{//}}$. In equation ***(5)***, the normal component ζ_z of $\boldsymbol{\zeta}$ is obtained using the following expression:

$$\zeta_z = -\left(\alpha\zeta_{inc,x} + \beta\zeta_{inc,y}\right) \Big/ (\varepsilon_{sub}k_0^2 - \alpha^2 - \beta^2)^{1/2} \qquad \textbf{(8)}$$

Finally, the electric intensity distributions generated in the simulated maps of the main manuscript and the figures S7 and S8 below take the following form:

$$I(\boldsymbol{r'}, \boldsymbol{r_0}, \omega) = |\boldsymbol{E}(\boldsymbol{r'}, \boldsymbol{r_0}, \omega)|^2 \qquad \textbf{(9)}$$

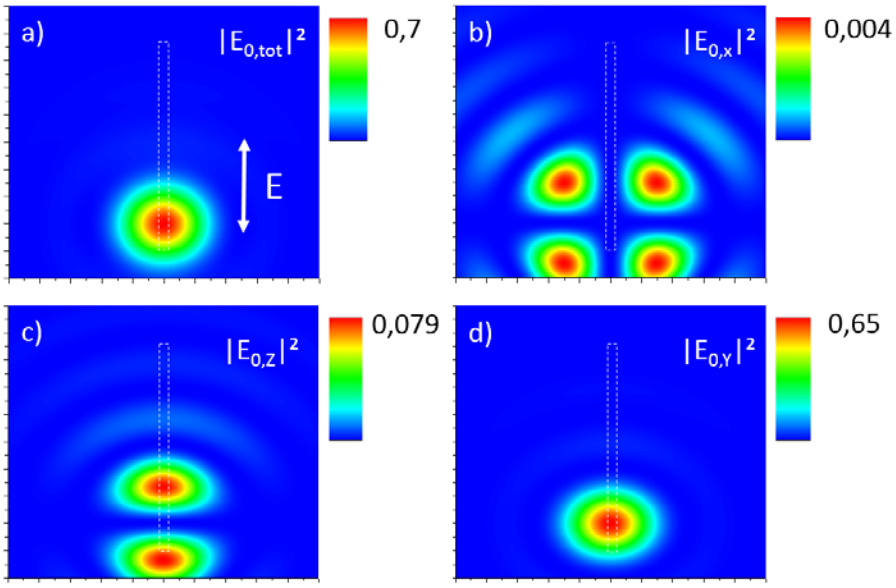

Figure S7. 2 x 2 µm² simulated images showing the normalized intensity distribution of the incident Gaussian illumination spot (a) Total normalized intensity for a polarization along the main axis of the wire. (b-d) Normalized intensity maps of the (b) x, (c) y and (d) z components of the field. The spot is placed at the location of one extremity of a 1.5-µm long, 50-nm diameter gold wire that is considered in Figure S8 and indicated here by the white dashed contour. In these simulations, the nanowire is not included.

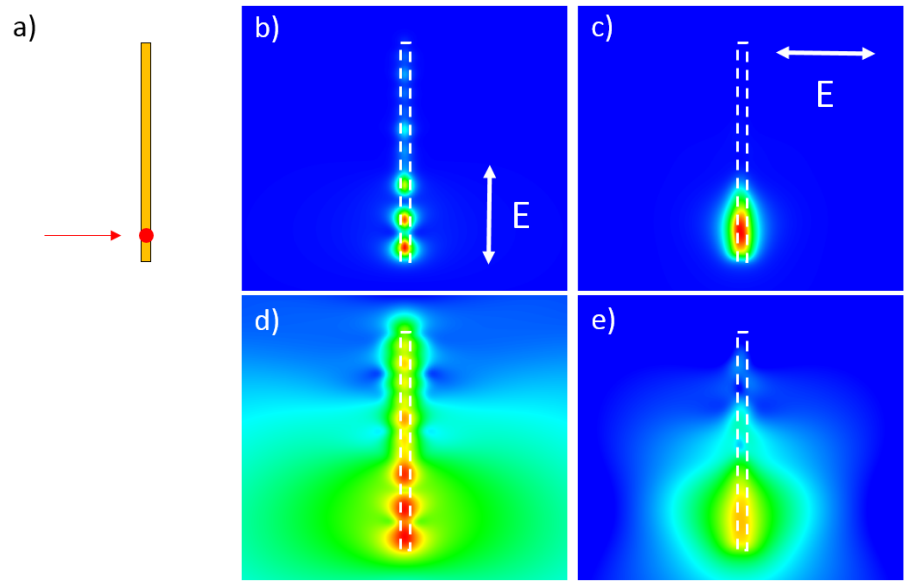

Figure S8. (a) Schematic view of the Gaussian excitation spot position (red dot) with respect to the 1.5 µm long gold wire. (b-c) Corresponding 2 x 2 µm² simulated images showing the intensity distribution of the total field propagating in the wire once illuminated by the Gaussian spot. (d-e) Similar to (b-c) with a logarithmic color scale. The incident polarization is indicated by the white arrows. The four maps are computed at a distance of 30 nm above the metallic wire.

S6 Resonant and non-resonant near-field transmittance maps and spectra in symmetrical diabolos

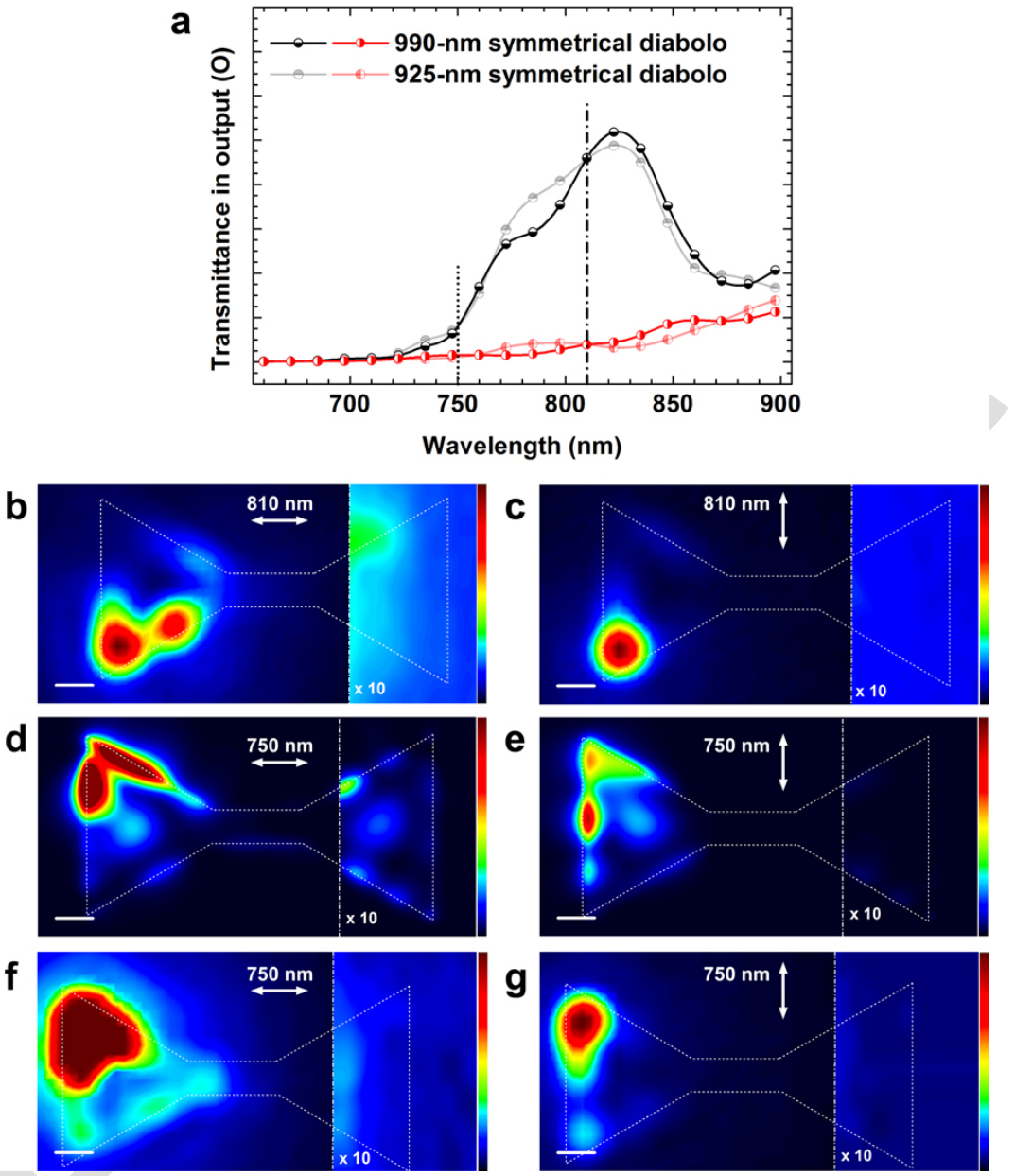

Figure S9: (a) Near-field transmittance spectra calculated at readout (O) for an excitation in (I) for the symmetrical diabolo with 990 nm sided triangular pads shown in Fig S1e. Horizontally (respectively vertically) split symbols correspond to the 0° (resp. 90°) polarization direction. The light-shaded spectra correspond to the symmetrical diabolo with 925-nm triangular pad studied in main text (See Fig. 5h). The dash-dotted and dotted lines indicate the experimental excitation wavelength (810 nm and 750 nm respectively). (b, c) Image plane TPL maps for the diabolo shown in Fig S1e obtained upon excitation in the lower left corner at 810 nm. (d, e) Transmittance maps for the diabolo shown in Fig S1e upon non-resonance excitation in (I) at 750 nm. (f, g) Image plane TPL maps for the diabolo shown in Fig S1e upon excitation in (I) at 750 nm. Scale bars are 200 nm. In maps in panels (b) to (g), the portion on the right of the dotted lines is plotted with a 10x magnified intensity using the same rainbow color scale.

The transmittance though mesoscopic symmetrical diabolo structures presents resonances in the visible and near-IR region as shown in Figure 6h. A small variation of the lateral size of the triangular pads has limited effect on the spectral characteristics of the transmittance modes. Indeed in Figure S9a, the transmittance of the diabolo structures shown in Fig. 2a and Fig. S1e, which have the same channel size but a pad size difference of ca. 70 nm, is virtually identical. In particular, the transmittance curves coincide at 810 nm (vertical dash-dot line in Fig. S9a). Experimentally, the image plane TPL maps recorded on the larger diabolo show significant transmittance when the excitation is polarized along the longitudinal direction (Fig. S9b) but none when the polarization is orthogonal to the main axis (Fig. S9c) as already described for the smaller diabolo in the main text (See Fig. 2d, e).

The spectra suggest that the transmittance can be spectrally suppressed for both polarizations by exciting the structures out of the resonances peaks, for example at the wavelength of 750 nm (dotted vertical line in Fig. S9a) where the spectral intensity is incidentally the same for both structures and low for both polarization.

Accordingly, simulated near-field transmission maps for an excitation in the upper left corner at a wavelength of 750 nm yields no or very small transmittance in the output (O) region for either 0° (Fig. S9d) or 90° (Fig. S9e) excitation polarization.

Experimental image plane TPL upon excitation at 750 nm are displayed in panels (f) and (g) of Figure S9. The patterns in the excitation pad match closely the simulated near-field and none of the two polarization conditions yields measurable transmittance as observed in the output region plotted with a 10x magnified color scale.

This further confirms the delocalized mode-mediated transmittance in the resonant diabolo structures.

S7 References

1. Viarbitskaya, S. et al. Morphology-induced redistribution of surface plasmon modes in two-dimensional crystalline gold platelets. *Applied Physics Letters* **103** (2013).
2. Viarbitskaya, S. et al. Tailoring and imaging the plasmonic local density of states in crystalline nanoprisms. *Nature Materials* **12**, 426-432 (2013).
3. Cuche, A. et al. Modal engineering of Surface Plasmons in apertured Au Nanoprisms. *Scientific Reports* **5** (2015).
4. Martin, O. J. F., Girard, C. & Dereux, A. Generalized field propagator for electromagnetic scattering and light confinement. *Physical Review Letters* **74**, 526-529 (1995).
5. Barchiesi, D., Girard, C., Martin, O. J. F., VanLabeke, D. & Courjon, D. Computing the optical near-field distributions around complex subwavelength surface structures: A comparative study of different methods. *Physical Review E* **54**, 4285-4292 (1996).
6. Arbouet, A., Mlayah, A., Girard, C. & des Francs, G. C. Electron energy losses and cathodoluminescence from complex plasmonic nanostructures: spectra, maps and radiation patterns from a generalized field propagator. *New Journal of Physics* **16**, 113012 (2014).
7. Torok, P., Varga, P. & Booker, G. R. Electromagnetic diffraction of light focused through a planar interface between materials of mismatched refractive indexes - Structure of the electromagnetic field. 1. *Journal of the Optical Society of America a-Optics Image Science and Vision* **12**, 2136-2144 (1995).
8. Torok, P., Varga, P., Konkol, A. & Booker, G. R. Electromagnetic diffraction of light focused through a planar interface between materials of mismatched refractive indices: Structure of the electromagnetic field .2. *Journal of the Optical Society of America a-Optics Image Science and Vision* **13**, 2232-2238 (1996).
9. Weeber, J. C., Dereux, A., Girard, C., Krenn, J. R. & Goudonnet, J. P. Plasmon polaritons of metallic nanowires for controlling submicron propagation of light. *Physical Review B* **60**, 9061-9068 (1999).
10. Teulle, A. et al. Scanning optical microscopy modeling in nanoplasmonics. *Journal of the Optical Society of America B-Optical Physics* **29**, 2431-2437 (2012).